AGU PUBLICATIONS

JGR

Journal of Geophysical Research: Solid Earth

RESEARCH ARTICLE

10.1002/2016JB013502

Key Points:
- Single-crystal X-ray diffraction experiments are carried out on aegirine [$NaFe^{3+}Si_2O_6$] at ambient temperature and high pressures to 60 GPa
- A second-order isosymmetric phase transition is detected and characterized by a discontinuity of bulk modulus
- If such clinopyroxenes can be preserved in cold subducted slab, the isosymmetric phase transition would cause an increase in buoyancy

Correspondence to:
P. K. Dera,
pdera@hawaii.edu

Citation:
Xu, J., D. Zhang, D. Fan, R. T. Downs, Y. Hu, and P. K. Dera (2017), Isosymmetric pressure-induced bonding increase changes compression behavior of clinopyroxenes across jadeite-aegirine solid solution in subduction zones, *J. Geophys. Res. Solid Earth*, *122*, 142–157, doi:10.1002/2016JB013502.

Received 30 AUG 2016
Accepted 20 NOV 2016
Accepted article online 23 NOV 2016
Published online 12 JAN 2017

Isosymmetric pressure-induced bonding increase changes compression behavior of clinopyroxenes across jadeite-aegirine solid solution in subduction zones

Jingui Xu[1,2,3], Dongzhou Zhang[2], Dawei Fan[1], Robert T. Downs[4], Yi Hu[2], and Przemyslaw K. Dera[2]

[1]Key Laboratory of High Temperature and High Pressure Study of the Earth's Interior, Institute of Geochemistry, Chinese Academy of Sciences, Guiyang, China, [2]Hawaii Institute of Geophysics and Planetology, School of Ocean and Earth Science and Technology, University of Hawai'i at Mānoa, Honolulu, Hawaii, USA, [3]University of Chinese Academy of Sciences, Beijing, China, [4]Department of Geosciences, University of Arizona, Tucson, Arizona, USA

Abstract Pyroxenes are among the most important minerals of Earth's crust and upper mantle and play significant role in controlling subduction at convergent margins. In this study, synchrotron-based single-crystal X-ray diffraction experiments were carried out on a natural aegirine [$NaFe^{3+}Si_2O_6$] sample at ambient temperature and high pressures to 60 GPa, simulating conditions within the coldest part of a subduction zone consisting of old lithosphere. The diffraction data reveal no obvious sign of structural phase transition in aegirine within this pressure range; however, several relevant structural parameter trends change noticeably at approximately 24 GPa, indicating the presence of the previously predicted isosymmetric bonding change, related to increase of coordination number of Na^+ at M2 site. The pressure-volume data, fit with third-order Birch-Murnaghan (BM3) equation of state over the whole pressure range, yields $K_{T0} = 126(2)$ GPa and $K'_{T0} = 3.3(1)$, while separate BM3 fits performed for the 0–24.0 GPa and 29.9–60.4 GPa pressure ranges give $K_{T0} = 118(3)$ GPa, $K'_{T0} = 4.2(3)$ and $K_{T0} = 133(2)$ GPa, $K'_{T0} = 3.0(1)$, suggesting that the structure stiffens as a result of the new bond formation. Aegirine exhibits strong anisotropic compression with unit strain axial ratios $\varepsilon_1:\varepsilon_2:\varepsilon_3 = 1.00:2.44:1.64$. Structural refinements reveal that NaO_8 polyhedron is the most compressible and SiO_4 tetrahedron has the lowest compressibility. The consequence of bonding transition is that the compressional behavior of aegirine below ~24 GPa and above that pressure is quite different, with likely consequences for relevant thermodynamic parameters and ion diffusion coefficients.

1. Introduction

Pyroxenes, with a general formula $M2M1T_2O_6$, where T are tetrahedral sites occupied predominantly by Si^{4+}; M1 are small octahedral cation sites, usually filled with Mg^{2+}, Fe^{2+}, and Fe^{3+}; and M2 are larger polyhedral sites that can accommodate variety of cations, are characterized by significant compositional and structural flexibility. Pyroxene minerals have been widely studied at high-pressure conditions because of their geological importance. They are among the most important minerals of Earth's crust and upper mantle and account for ~20% by volume of pyrolytic upper mantle mineral constituents [*Frost*, 2008; *Ringwood*, 1975]. Moreover, pyroxenes are major constituents of harzburgite and lherzolite which are important petrological components of subducting slabs [*Ringwood*, 1982; *Stixrude and Lithgow-Bertelloni*, 2007]. Generally, pyroxene group minerals crystallize in either monoclinic or orthorhombic systems. Orthopyroxenes transform to monoclinic $C2/c$ symmetry at P-T conditions equivalent to ~225 km depth, which is regarded as one possible candidate to explain the mantle "X discontinuity" [*Akashi et al.*, 2009; *Woodland*, 1998; *Woodland and Angel*, 1997]. Recent studies suggest that the pressure-induced structural transitions of orthopyroxenes are more complex than previously thought. At lower temperatures orthopyroxenes can transform to structures different from the $C2/c$ symmetry at high pressures [*Dera et al.*, 2013a; *Finkelstein et al.*, 2015; *Jahn*, 2008; *Kung et al.*, 2004; *Zhang et al.*, 2011, 2012], and their structural transitions might be sensitive to the stress environment [*Zhang et al.*, 2011]. $P2_1/c$ monoclinic pyroxene has a low shear velocity profile [*Kung et al.*, 2004; *Zhang et al.*, 2013], which might explain the features of some regional seismic observations [*Zhang et al.*, 2013]. At depths of the transition zone, pyroxenes dissolve into garnet [*Ringwood*, 1967] or decompose into spinel plus stishovite [*Akimoto and Syono*, 1970; *Liu*, 1976a; *Ming and Bassett*, 1975]. However, metastable phases of pyroxenes may be preserved in cold subducting slabs and pass through the transition zone to greater depths,

Table 1. Structural Refinement Details of Aegirine at Different Pressures up to 60.4 GPa

Pressure (GPa)	0.0001	1.9(1)	5.9(1)	12.7(1)	18.6(1)
R_{int} (%)	5.54	7.39	9.69	8.94	9.83
R_1 (all reflections, %)	4.88	4.85	5.23	5.01	4.97
R_1 (Fo > 4sig(Fo))	4.88	4.46	4.27	4.88	4.97
wR_2 (all reflections, %)	12.09	11.39	8.51	10.91	12.01
Goodness of fit	1.047	1.129	1.104	1.166	1.155
No. of total reflections	2645	433	343	317	291
No. of reflections (Fo > 4sig(Fo))	555	191	154	137	127
No. of fitting parameters	24	24	24	24	24
Pressure (GPa)	24.0(1)	29.9(1)	40.7(1)	44.5(1)	60.4(1)
R_{int} (%)	8.85	8.06	8.13	8.69	9.30
R_1 (all reflections, %)	4.79	5.01	4.90	4.90	4.95
R_1 (Fo > 4sig (Fo))	4.76	4.99	4.88	4.90	4.95
wR_2 (all reflections, %)	10.13	12.19	11.17	10.31	10.05
Goodness of fit	1.178	1.140	1.095	1.057	1.266
No. of total reflections	427	332	325	332	260
No. of reflections (Fo > 4sig(Fo))	183	138	135	141	109
No. of fitting parameters	24	24	24	24	24

given the condition that the pyroxene-garnet reaction is suppressed at lower temperatures [*Agrusta et al*., 2014; *King et al*., 2015; *Nishi et al*., 2008, 2013; *Van Mierlo et al*., 2013]. As pressure increases, decomposition requires higher temperatures because of the positive Clapeyron slope [*Akimoto and Syono*, 1970]. Such cold conditions could be present in old and rapidly subducting slabs because the thermal evolution of the slab is strongly affected by its rate and age [*Bina and Navrotsky*, 2000]. For instance, a relatively low temperature (~1000 K) can be retained to a depth of ~800 km [*Bina et al*., 2001]. Therefore, it is important to investigate the high-pressure behavior of pyroxenes at relatively low temperature to understand the geophysical and geochemical properties of subduction zones [*Akashi et al*., 2009; *Bina et al*., 2001]. Aegirine [$NaFe^{3+}Si_2O_6$] is an important member of the clinopyroxene group and occurs in alkalic igneous and blueschist facies rocks [*Angiboust et al*., 2016]. It forms solid solution with jadeite and can be enriched in augite [*Cortesogno et al*., 2002]. High-pressure studies of aegirine can be useful to constrain the behaviors of clinopyroxene solutions. Aegirine has been investigated in several studies at high-pressure or high-temperature conditions since *Clark et al*. [1969] first reported the crystal structure. *Cameron et al*. [1973] investigated the structural evolution of aegirine at high temperatures up to 800°C and found that the bond length (Na-O and Fe-O) increased linearly with temperature. The high-pressure equation of state of aegirine has been studied by *Downs and Singh* [2006] and *Nestola et al*. [2006] to 11.55 and 9.74 GPa, respectively. *McCarthy et al*. [2008a] performed structural refinements of aegirine at high pressures to 11.55 GPa and inferred that the $C2/c \rightarrow C2/c$ bonding transition of aegirine should take place at ~20 GPa. All of these studies of aegirine at high pressures show that no phase transition occurs within the pressure ranges (0–12 GPa); however, geometric analysis of coordination geometry trends [*McCarthy et al*., 2008a; *McCarthy et al*., 2008b] predicted that both jadeite and aegirine should undergo a coordination number increase at the M2 site at pressure around 20 GPa. To better understand the structural evolution and the possible bonding transitions of metastable aegirine at transition zone conditions, it is necessary to investigate its response to much higher pressures. In the current study we investigated the compressional behavior of aegirine to ~60 GPa at ambient temperature in a diamond anvil cell (DAC), using in situ synchrotron single-crystal X-ray diffraction.

2. Sample and Experimental Methods

A natural sample of aegirine was obtained from the University of Arizona RRUFF collection (rruff.info/#R050074). The sample's composition was determined as $(Na_{.98}Ca_{.02})(Fe^{3+}_{.96}Ti_{.01}Mn_{.03})Si_{2.00}O_6$, based on electron microprobe analysis. A small chip of aegirine single crystal with a thickness of less than 10 μm, extracted from a larger specimen, was used for our experiments. A BX90 DAC was used to generate high-pressure conditions [*Kantor et al*., 2012]. The BX90 DAC had a ±25° opening angle and was equipped with two type-I diamond anvils (300 μm diameter culet) and WC seats. A rhenium foil, preindented to thickness of ~45 μm, was used as a gasket, and a hole of 180 μm in diameter was drilled to serve as the sample chamber. The selected sample and a small ruby sphere (~10 μm in diameter) were loaded into the sample

Table 2. Unit Cell Parameters of Aegirine at Ambient and High Pressures

P(GPa)	*a* (Å)	*b* (Å)	*c* (Å)	β (deg)	*V* (Å^3)
0.0001	9.676(1)	8.8203(8)	5.2942(5)	107.24(1)	431.5(1)
1.9(1)	9.633(4)	8.7597(38)	5.2657(9)	107.01(2)	424.9(3)
5.9(1)	9.525(6)	8.6610(50)	5.2159(9)	106.60(2)	412.4(3)
12.7(1)	9.415(9)	8.5198(90)	5.1315(20)	106.06(5)	395.6(6)
18.6(1)	9.346(8)	8.3479(77)	5.0873(17)	105.76(4)	382.0(5)
24.0(1)	9.257(7)	8.2617(58)	5.0509(14)	105.65(4)	371.9(4)
29.9(1)	9.203(8)	8.1527(74)	5.0078(18)	105.27(5)	362.5(5)
40.7(1)	9.108(8)	7.9610(70)	4.9431(18)	105.47(5)	345.4(5)
44.5(1)	9.063(8)	7.9079(76)	4.9157(20)	105.34(5)	339.7(5)
54.3(1)	9.016(7)	7.7494(57)	4.8585(17)	104.95(5)	328.0(4)
60.4(1)	8.970(6)	7.6396(55)	4.8439(15)	105.32(4)	320.1(3)

chamber, and then the sample chamber was filled with neon as the pressure transmitting medium using the GSECARS gas loading system [*Rivers et al.*, 2008]. A small ruby sphere was employed to determine pressure in the sample chamber [*Mao et al.*, 1986].

Ambient-condition single-crystal X-ray diffraction experiment was carried out at the experiment station 13-BM-C of the Advanced Photon Source, Argonne National Laboratory. The incident X-ray beam had a wavelength of 0.4340 Å and a focal spot size of $15 \times 15\ \mu m^2$ full width at half maximum (FWHM). Diffraction images were acquired with a MAR165 CCD detector. LaB_6 powder was used as the diffraction standard. Wide and stepped ϕ exposures were collected in a rotation range from $-90°$ to 90°, and the exposure time was 1 s/deg. High-pressure single-crystal X-ray diffraction experiments were carried out at the experimental station 13-ID-D. The incident X-ray beam was monochromated to a wavelength of 0.3344 Å and focused to a spot size of $4 \times 4\ \mu m^2$ FWHM. Diffraction images were acquired with a MAR165 CCD detector (Rayonix). The tilting and the distance of the detector relative to the X-ray beam were calibrated by using LaB_6 powder as the diffraction standard. The ω scan rotation axis was vertical and perpendicular to the incident X-ray direction. Wide and stepped exposures were collected at each pressure at three detector positions (D1, D2, and D3), achieved by translating the detector horizontally by ± 70 mm. Full-rotation exposures with exposure time of 1 s/deg were performed at D1 position, in addition to step exposures with 1° rotation steps. At D2 and D3 positions, wide segment exposures with 12° rotation steps were collected after full-rotation exposures, and the exposure time of both was 0.5 s/deg.

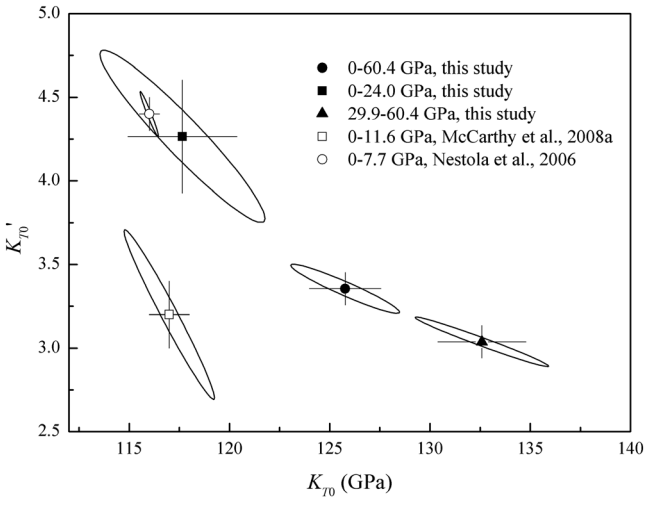

Figure 1. Isothermal bulk moduli and their pressure derivatives of aegirine in this and previous studies. The values of isothermal bulk moduli and their pressure derivatives are $K_{T0} = 117(1)$ GPa and $K'_{T0} = 3.2(2)$ [*McCarthy et al.*, 2008a], $K_{T0} = 116.1(5)$ GPa and $K'_{T0} = 4.4(1)$ [*Nestola et al.*, 2006], $K_{T0} = 126(2)$ GPa and $K'_{T0} = 3.4(1)$ (this study, whole P range) and $K_{T0} = 118(3)$ GPa and $K'_{T0} = 4.3(3)$ (low P range), and $K_{T0} = 133(2)$ GPa and $K'_{T0} = 3.0(1)$ (high P range).

Diffraction images were analyzed by using the ATREX/RSV software package [*Dera et al.*, 2013b]. Peak intensities were corrected for polarization, Lorentz, and DAC absorption. The lattice parameters and orientation matrix were determined with the RSV software [*Dera et al.*, 2013b]. Crystal structures at high pressures were refined from the intensity data with SHELXL software, facilitated by WINGX and Olex2 user interfaces [*Dolomanov et al.*, 2009; *Farrugia*, 2012; *Sheldrick*, 2007]. According to the microprobe analysis, we assumed that the M2 sites were fully occupied by Ca^{2+} (2%, apfu) and Na^{+} (98%), while Fe^{3+} (96%), Mn^{3+} (3%), and Ti^{4+} (1%) occupied the M1 sites, and the T sites only contained Si^{4+}. We did not refine the site occupancy factors. The atomic displacement

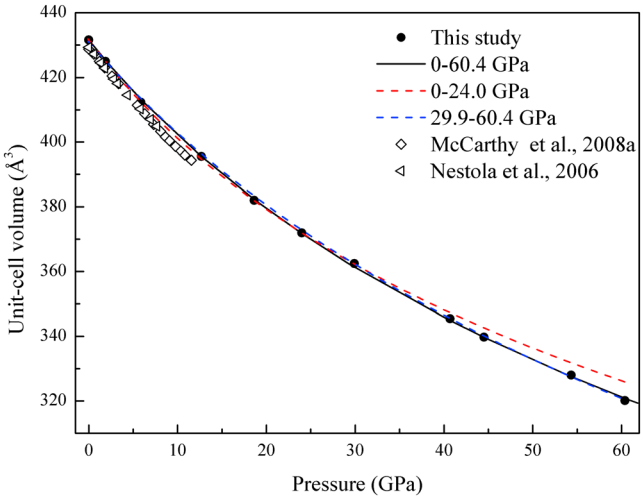

Figure 2. Unit cell volume of aegirine as a function of pressure and EoS fitting curves based on different data ranges. The error bars of the data points are smaller than the symbols. (*Color online*).

parameters (ADPs) of M1 site were set to be anisotropic, while M2 were kept isotropic. Cations occupying the same polyhedral site were set to share the same ADP values and the same fractional coordinates. Details of the crystal structural refinement at different pressures (except for 54.3(1) GPa) are given in Table 1. We did not refine the structure at 54.3(1) GPa because the crystal position drifted during the exposure, yet the lattice parameters at 54.3(1) GPa were used to calculate the sample's equation of state.

3. Results and Discussion

3.1. Equation of State of Aegirine

Unit cell parameters of aegirine to ~60 GPa are summarized in Table 2. Pressure-volume equation of state for aegirine was obtained by fitting a third-order Birch-Murnaghan equation (BM3):

$$P = (3/2)K_{T0}\left[(V_0/V)^{7/3} - (V_0/V)^{5/3}\right] \times \left[1 + (3/4)(K'_{T0} - 4)\left[(V_0/V)^{2/3} - 1\right]\right] \quad (1)$$

where V_0, V, K_0, and K'_0 are the ambient pressure volume, high-pressure volume, isothermal bulk modulus, and its pressure derivative, respectively, using the console program, EosFit7c [*Angel et al.*, 2014]. Using BM3 equation for all available pressure points we obtained $K_{T0} = 126(2)$ GPa and $K'_{T0} = 3.3(1)$. Second-order Birch-Murnaghan equation of state fit yielded $K_{T0} = 116(1)$ GPa and $K'_{T0} = 4$. The BM3 K_{T0} value of this study is much higher than the results from *Nestola et al.* [2006] (116.1 (5) GPa) and *McCarthy et al.* [2008a] (117 (1) GPa) (Figure 1). We attribute this discrepancy to the change of compression mechanism at 24 GPa. We also performed separate BM3 fits of data below and above 24 GPa. V_0 was fixed to the measured ambient pressure value for both pressure regions, because of limited number of pressure point available. The resulting bulk moduli, $K_{T0} = 118(3)$ GPa, $K'_{T0} = 4.3(3)$ and $K_{T0} = 133(2)$ GPa, $K'_{T0} = 3.0(1)$, indicate that aegirine becomes stiffer after the bonding change. It should be noted that the K_{T0} value derived from data below 24 GPa is also slightly higher than that of *Nestola et al.* [2006] (116.1 (5) GPa) and *McCarthy et al.* [2008a] (117(1) GPa) (Figure 1). We attribute this minor discrepancy to the compositional differences, the aegirine sample used in this study is natural, while *Nestola et al.* [2006] and *McCarthy et al.* [2008a] used purely synthetic samples. The natural aegirine has Mn^{3+} and Ti^{3+} in M1 site, except for Fe^{3+}, and Ca^{2+} substitution in M2 site. At ambient conditions the effective ionic radius of Mn^{3+} (0.645 Å) is identical to Fe^{3+} (0.645 Å), Ti^{3+} (0.670 Å) is larger than Fe^{3+} and Mn^{3+}, and Ca^{2+} (1.12 Å) are smaller than Na^{+} (1.18 Å) [*Shannon*, 1976]. Normally, larger metal cations cause higher compressibilities for *C2/c* clinopyroxenes

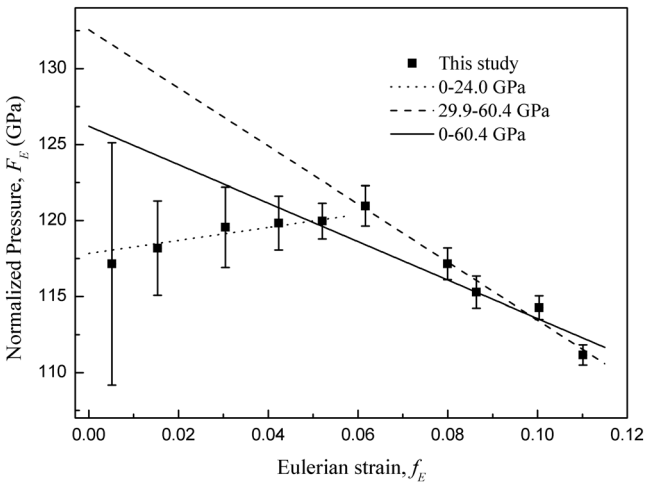

Figure 3. Eulerian strain-normalized pressure (f_E-F_E) plot of unit cell volume. Linear fits of the data from different pressure range yield the intercept values of $F_{EV}(0) = 126(2)$ GPa (all data), 117.8(5) GPa (low pressure), and 133(2) GPa (high pressure).

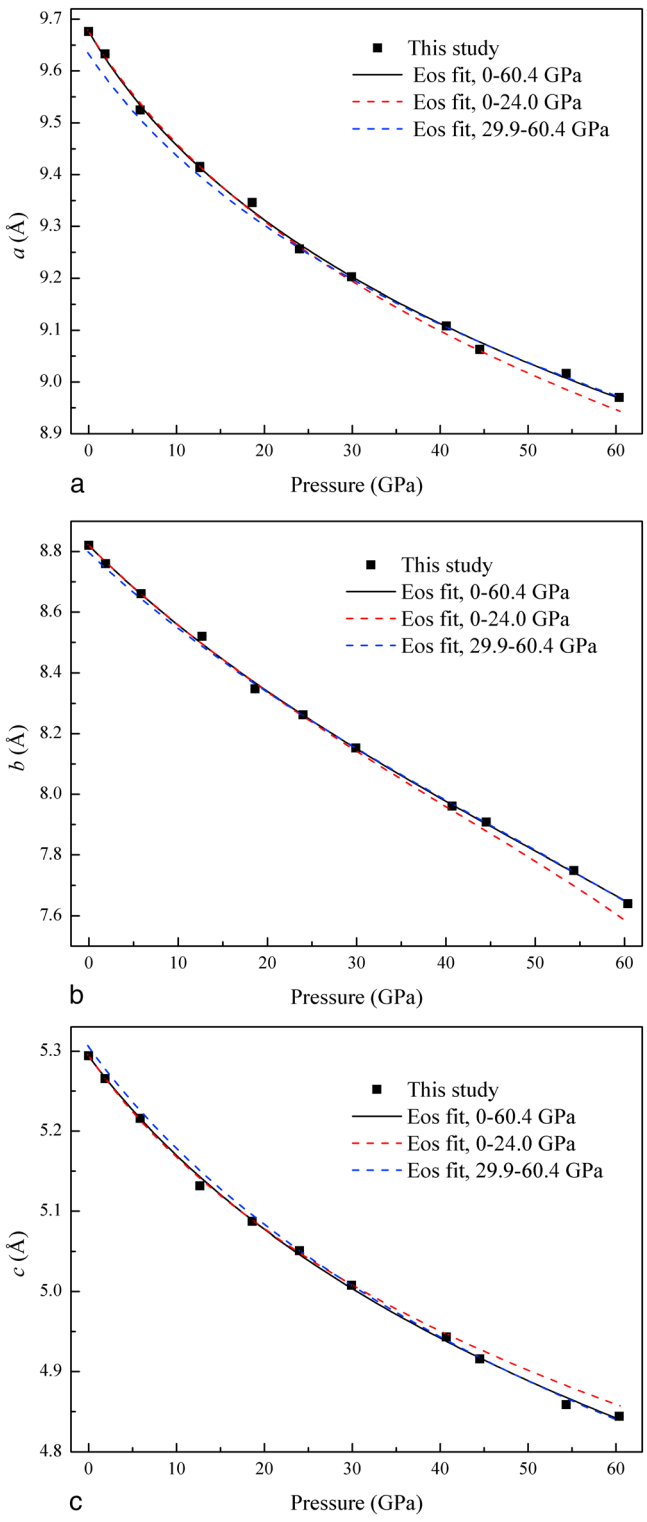

Figure 4. Pressure dependence of the lattice parameters of aegirine in this study. The error bars of the data points are smaller than the symbols. (*Color online*).

[e.g., *Nestola et al.*, 2010], and Ca^{2+} content is higher than Ti^{3+} [$(Na_{.98}Ca_{.02})(Fe^{3+}_{.96}Ti_{.01}Mn_{.03})Si_{2.00}O_6$], which could result in a slightly higher K_{T0} value of this natural aegirine sample. The Vinet equation of state (EoS) [*Vinet et al.*, 1986; *Vinet et al.*, 1987] was also used to analyze the *P-V* data. The expression for the Vinet EoS is $P(V) = 3K_0y^{-2}(1-y)\exp[\eta_0(1-y)]$, where $y = x^{1/3}$, $x = V/V_0$, and $\eta_0 = (3/2)(K'_0 - 1)$. Vinet EoS analyses yield the values of $K_0 = 117(3)$ GPa and $K'_0 = 4.4(4)$ for 0–24 GPa and $K_0 = 134(3)$ GPa and $K'_0 = 2.9(2)$ for the rest of the pressure range. These values are close to that derived by the fitting to BM EoS within their uncertainty. The *P-V* data and the fitted curves are plotted in Figure 2. Figure 3 shows the dependence of volume Eulerian finite strain ($f_E = [(V_0/V)^{2/3} - 1]/2$) and normalized stress ($F_E = P/[3f_E(2f_E + 1)^{5/2}]$) [*Angel*, 2000]. We note that the f_E-F_E plot exhibits clearly distinct regions of compressional behavior. Data at low strains, below 24 GPa, have a positive slope, and intercept at approximately 117 GPa, in agreement with earlier, lower pressure studies, whereas data at high strains show clear negative slope. Weighted linear fit of all data points yields the intercept value of 126(2) GPa which is in good agreement with the result of BM3 fitting discussed above, whereas separate linear fits for the two distinct compression regimes give intercepts of 117.8(5) GPa and 133(2) GPa, respectively. The evolution of unit cell parameters *a*, *b*, and *c* as functions of pressure shows a large anisotropy. Parameters *a* and *c* decrease with increasing pressure and exhibit nonlinear trend, while *b* decreases with significant linearity (Figure 4). The β angle decreases monotonically with pressure up to ~24 GPa, then becomes almost constant upon further compression (Figure 5).

Unit-cell parameters were used to analyze unit strain ellipsoid with win_STRAIN, developed by Dr. Ross Angel, modified after *Ohashi* [1982].

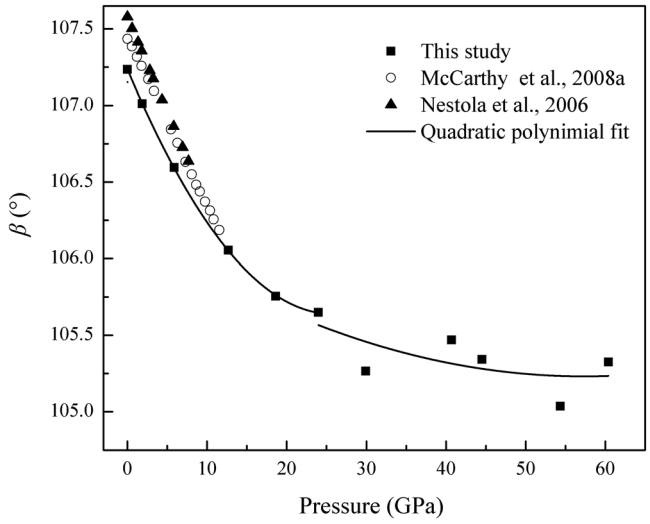

Figure 5. Pressure dependence of β angle of aegirine. The error bars of the data points are smaller than the symbols.

The results indicate that the unit strain ellipsoid is highly anisotropic. In the range of 0–60.4 GPa, the axial lengths of the strain ellipsoid are ε_1, −0.058427; ε_2, −0.142611; and ε_3, −0.095615 GPa^{-1}, with ε_3 inclined at 154.4° with respect to (001) and ε_2 parallel to (010). The axial ratio of ε_1:ε_2:ε_3 is 1.00:2.44:1.64. The axial ratios determined by *Nestola et al.* [2006] and *McCarthy et al.* [2008b] are 1.00:2.38:2.76 (0–5.79 GPa) and 1.00:2.38:2.63 (0–11.55 GPa), respectively, which are different from our results. This difference again implies that the compression mechanism of aegirine changes at higher pressures. The ε_3 is closer to ε_1 in this study, while ε_2 is consistent with previous studies.

3.2. Polyhedral Compression and Distortion

The fractional coordinates of atoms in aegirine are listed in Table 3. Bond lengths, angles, and polyhedral volumes are shown in Tables 4–6 and Figures 6–8. The bond nomenclature used in this study is adopted after *Zhang et al.* [1997]. The compressibilities of the three polyhedra (NaO_8, FeO_6, and SiO_4) are significantly different.

3.2.1. NaO_8

At ambient conditions there are only three unique pairs of Na-O bonds in aegirine, according to procrystal electron density distribution analysis [*Downs*, 2003], and Na is not bonded to O3(C2) and O3(D2). All Na-O

Table 3. Fractional Coordinates and Displacement Parameters of Atoms in Aegirine at Different Pressures

	Pressure (GPa)	0.0001	1.9(1)	5.9(1)	12.7(1)	18.6(1)	24.0(1)	29.9(1)	40.7(1)	44.5(1)	60.4(1)
Na	X	0	0	0	0	0	0	0	0	0	0
	Y	0.3003(3)	0.3026(7)	0.3024(7)	0.3087(7)	0.3094(9)	0.3114(6)	0.3127(6)	0.3159(8)	0.3164(7)	0.3210(12)
	Z	0.2500	0.2500	0.2500	0.2500	0.2500	0.2500	0.2500	0.2500	0.2500	0.2500
	Uiso	0.0120(5)	0.0121(10)	0.0124(10)	0.0088(13)	0.0040(13)	0.0061(8)	0.0055(8)	0.0040(9)	0.0064(9)	0.0195(16)
Fe	X	0	0	0	0	0	0	0	0	0	0
	Y	0.8993(1)	0.9001(2)	0.9001(2)	0.9032(3)	0.9039(4)	0.9045(2)	0.9052(2)	0.9053(3)	0.9055(3)	0.9054(4)
	Z	0.2500	0.2500	0.2500	0.2500	0.2500	0.2500	0.2500	0.2500	0.2500	0.2500
	Uiso	0.0071(2)	0.0068(4)	0.0069(4)	0.0062(6)	0.0058(7)	0.0068(4)	0.0076(5)	0.0061(6)	0.0068(5)	0.0052(7)
Si	X	0.2903(1)	0.2902(2)	0.2903(2)	0.2916(3)	0.2912(4)	0.2921(2)	0.2921(3)	0.2920(3)	0.2922(3)	0.2914(4)
	Y	0.0898(1)	0.0904(3)	0.0903(3)	0.0933(4)	0.0936(5)	0.0949(3)	0.0944(2)	0.0962(4)	0.0959(3)	0.0962(5)
	Z	0.2351(2)	0.2354(4)	0.2355(4)	0.2381(5)	0.2399(6)	0.2416(4)	0.2431(3)	0.2481(5)	0.2499(4)	0.2598(6)
	Uiso	0.0062(2)	0.0052(4)	0.0053(4)	0.0058(6)	0.0057(7)	0.0045(4)	0.0047(5)	0.0044(6)	0.0029(5)	0.0054(7)
O1	X	0.1140(3)	0.1139(7)	0.1141(7)	0.1145(9)	0.1119(10)	0.1126(6)	0.1130(7)	0.1117(9)	0.1108(8)	0.1101(10)
	Y	0.0796(3)	0.0788(8)	0.0790(8)	0.0825(10)	0.0848(12)	0.0885(8)	0.0920(7)	0.0940(10)	0.0939(9)	0.1063(13)
	Z	0.1393(6)	0.1400(11)	0.1402(11)	0.1393(13)	0.1398(14)	0.1416(10)	0.1388(10)	0.1434(15)	0.1405(13)	0.1429(14)
	Uiso	0.0074(5)	0.0067(10)	0.0066(10)	0.0074(13)	0.0049(14)	0.0067(9)	0.0095(12)	0.0084(14)	0.0065(11)	0.0023(15)
O2	X	0.3585(4)	0.3574(7)	0.3569(7)	0.3573(9)	0.3537(11)	0.3558(7)	0.3540(7)	0.3529(9)	0.3511(8)	0.3511(11)
	Y	0.2551(4)	0.2566(9)	0.2567(9)	0.2636(10)	0.2693(13)	0.2683(7)	0.2695(7)	0.2728(11)	0.2779(11)	0.2834(14)
	Z	0.3021(7)	0.3052(12)	0.3047(12)	0.3237(14)	0.3264(16)	0.3338(11)	0.3396(11)	0.3491(14)	0.3488(13)	0.3636(14)
	Uiso	0.0107(6)	0.0102(11)	0.0103(11)	0.0069(14)	0.0097(17)	0.0067(9)	0.0082(10)	0.0064(13)	0.0089(10)	0.0019(16)
O3	X	0.3520(4)	0.3535(7)	0.3534(7)	0.3567(8)	0.3561(10)	0.3578(6)	0.3611(5)	0.3641(7)	0.3649(7)	0.3656(11)
	Y	0.0085(4)	0.0109(8)	0.0105(8)	0.0213(10)	0.0238(12)	0.0287(7)	0.0300(9)	0.0349(10)	0.0333(10)	0.0385(12)
	Z	0.0112(7)	0.0107(12)	0.0106(12)	0.0003(14)	-0.0048(15)	-0.0031(10)	-0.0016(9)	0.0001(12)	0.0039(12)	0.0076(16)
	Uiso	0.0101(5)	0.0064(10)	0.0067(10)	0.0060(12)	0.0050(14)	0.0047(8)	0.0066(10)	0.0015(10)	0.0033(9)	0.0065(17)

Table 4. Selected Bond Lengths (Å) and Angles (deg), Polyhedral Volume (Å^3), and Distortion Parameters for NaO_8 Polyhedron in Aegirine at Pressures up to 60.4 GPa

Pressure (GPa)	0.0001	1.9(1)	5.9(1)	12.7(1)	18.6(1)	24.0(1)	29.9(1)	40.7(1)	44.5(1)	60.4(1)
Na-O1(A1, B1) × 2	2.394(4)	2.398(9)	2.364(9)	2.353(10)	2.312(8)	2.263(6)	2.242(6)	2.192(7)	2.204(7)	2.051(12)
Na-O2(C2, D2) × 2	2.411(4)	2.402(6)	2.378(6)	2.311(7)	2.289(12)	2.255(8)	2.221(7)	2.172(10)	2.163(9)	2.145(8)
Na-O3(C1, D1) × 2	2.439(4)	2.425(8)	2.417(8)	2.405(9)	2.397(11)	2.384(7)	2.379(6)	2.299(7)	2.297(7)	2.227(9)
Na-O3(C2, D2) × 2	2.825(4)	2.772(7)	2.677(7)	2.555(8)	2.493(10)	2.433(6)	2.347(8)	2.298(9)	2.263(9)	2.201(11)
Mean bond length	2.5173	2.4995	2.459	2.4062	2.3729	2.3337	2.2974	2.2405	2.232	2.1559
Volume	26.2583	25.8430	24.7381	23.3332	22.5285	21.5165	20.6108	19.2492	19.0503	17.3804
Distortion index	0.06112	0.05457	0.04428	0.03084	0.03035	0.03199	0.0287	0.02605	0.0216	0.02691

distances decrease with pressure. The longest (unbonded) Na-O3(C2, D2) distance experiences the highest compression, reaching 13.88% at 24.0(1) GPa, but after it becomes comparable to the other Na-O bonds, the gradient of the distance compression decreases, indicating emergence of new type if interaction. Na-O1(A1, B1) and Na-O2(C2, D2) are shortened by 14.33% and 11.03%, respectively. Na-O3(C1, D1) is the most incompressible bond in this polyhedron and shortened by 8.69% (Figure 6 and Table 4). The mean bond length is shortened by 14.36%.

3.2.2. $Fe^{3+}O_6$

Three bond pairs display the same evolution trend through the whole pressure range (Figure 7 and Table 5). The longest bond Fe-O1(A1,B1) compresses by 6.95%. Fe-O1(A2, B2) and Fe-O2(C1, D1) bonds are compressed by 6.72 and 6.06%, respectively. The mean bond length is shortened by 6.60%.

3.2.3. SiO_4

There are four different bonds in SiO_4 tetrahedron (Figure 8 and Table 6). In the whole pressure range, Si-O1(C1), Si-O3(C1), and Si-O3(C2) exhibit similar compressions of ~3%, while Si-O2(C1) is stiffer and has a compression of ~2%. The compression of the mean Si-O bond length is ~3%.

The distortion index (D) describes polyhedral distortion [*Baur*, 1974; *Robinson et al*., 1971], defined as $D = \frac{1}{n}\sum_{i=1}^{n}\frac{l_i - l_{av}}{l_{av}}$, where l_i is the distance from the central cation to the ith surrounding oxygen and l_{av} is the average distance. In this study, we found the NaO_8 polyhedra to have the maximum distortion indices, while the SiO_4 tetrahedra have the minimum distortion through the whole pressure range. Moreover, the distortion indices of SiO_4 tetrahedra and FeO_6 octahedra are not very responsive to pressure changes, while the distortion indices of NaO_8 polyhedra decrease significantly from 0 GPa to 12.7(1) GPa (Figure 9).

Bond angle variance (σ^2) and quadratic elongation (λ) are employed to describe the deviation from the perfect polyhedral shape (polyhedra with regular shape) [*Robinson et al*., 1971]. The angle variance and

Table 5. Selected Bond Lengths (Å) and Angles (deg), Polyhedral Volume (Å3), and Distortion Parameters for FeO_6 polyhedron in Aegirine at Pressures up to 60.4 GPa

Pressure (GPa)	0.0001	1.9(1)	5.9(1)	12. 7(1)	18.6(1)	24.0(1)	29.9(1)	40.7(1)	44.5(1)	60.4(1)
Fe-O1(A1, B1) × 2	2.115(3)	2.089(7)	2.071(8)	2.039(9)	2.002(10)	2.001(7)	2.004(6)	1.964(8)	1.950(8)	1.968(10)
Fe-O1(A2, B2) × 2	2.038(3)	2.036(6)	2.009(6)	1.994(7)	1.977(7)	1.972(5)	1.951(5)	1.939(7)	1.917(6)	1.901(7)
Fe-O2(C1, D1) × 2	1.947(4)	1.944(8)	1.933(8)	1.909(9)	1.889(11)	1.879(6)	1.884(6)	1.870(8)	1.850(8)	1.829(10)
Mean bond length	2.0332	2.0231	2.0047	1.9806	1.9561	1.951	1.9463	1.9244	1.9056	1.899
O1(A1)-Fe-O1(B1)	82.5(2)	82.9(4)	82.2(4)	82.9(5)	82.0(5)	81.2(3)	81.1(3)	80.2(4)	80.4(4)	77.4(5)
O1(A1)-Fe-O1(A2) × 2	92.4(1)	92.2(3)	93.3(3)	93.0(3)	94.0(4)	94.5(2)	95.1(2)	95.5(4)	95.9(3)	97.8(4)
O1(A1)-Fe-O1(B2) × 2	79.7(1)	79.9(3)	80.5(3)	81.7(3)	81.8(4)	82.9(3)	83.9(3)	84.2(4)	83.9(3)	86.4(4)
O2(C1)-Fe-O1(A1) × 2	90.3(1)	90.7(2)	90.5(2)	91.2(3)	91.1(4)	90.4(2)	89.7(2)	87.7(3)	87.9(3)	84.4(3)
O2(C1)-Fe-O1(A2) × 2	90.6(1)	89.4(3)	89.2(3)	87.5(4)	85.9(5)	86.5(3)	85.7(2)	84.4(3)	83.1(3)	82.0(4)
O2(D1)-Fe-O1(A2) × 2	96.3(1)	96.0(3)	94.8(3)	93.1(3)	92.1(4)	91.6(2)	91.1(2)	92.5(3)	92.2(3)	92.9(3)
O2(C1)-Fe-O2(D1)	98.5(2)	99.7(4)	100.8(4)	102.9(5)	107.1(7)	106.4(4)	108.1(4)	111.3(5)	113.9(5)	118.7(6)
Volume	11.0182	10.8545	10.5621	10.195	9.7616	9.7037	9.6166	9.2304	8.9112	8.6907
Distortion index	0.02819	0.02595	0.02374	0.02413	0.02273	0.02446	0.02145	0.01876	0.01951	0.02458
Quadratic elongation, λ	1.0126	1.0123	1.0122	1.0114	1.0154	1.0143	1.0154	1.0199	1.024	1.0344
Bond angle variance, σ^2	39.0848	39.1541	38.833	36.9622	51.5764	47.2387	52.0485	69.5054	83.8445	121.3496

Table 6. Selected Bond Lengths (Å) and Angles (deg), Polyhedral Volume (Å3), and Distortion Parameters for SiO_4 tetrahedron in Aegirine at Pressures up to 60.4 GPa

Pressure (GPa)	0.0001	1.9(1)	5.9(1)	12.7(1)	18.6(1)	24.0(1)	29.9(1)	40.7(1)	44.5(1)	60.4(1)
Si-O1(C1)	1.632(4)	1.625(7)	1.620(8)	1.606(8)	1.608(9)	1.602(6)	1.593(7)	1.585(9)	1.589(7)	1.576(9)
Si-O2(C1)	1.596(4)	1.593(8)	1.588(9)	1.591(9)	1.597(12)	1.571(7)	1.566(6)	1.545(8)	1.567(9)	1.562(11)
Si-O3(C1)	1.642(3)	1.637(6)	1.636(6)	1.629(7)	1.615(9)	1.613(5)	1.610(5)	1.613(6)	1.601(6)	1.588(9)
Si-O3(C2)	1.652(4)	1.656(7)	1.652(8)	1.638(8)	1.634(8)	1.629(6)	1.625(6)	1.624(8)	1.613(7)	1.599(8)
Mean bond length	1.6303	1.6278	1.6237	1.6159	1.6134	1.6037	1.5982	1.5915	1.5925	1.5815
O1(C1)-Si-O2(C1)	116.4(2)	116.4(3)	115.4(3)	115.5(4)	108.0(5)	113.5(3)	111.9(3)	111.5(4)	110.6(4)	107.7(5)
O1(C1)-Si-O3(C1)	108.5(2)	108.5(3)	110.0(4)	110.2(4)	108.1(5)	108.7(3)	114.0(3)	110.2(4)	109.7(3)	119.3(5)
O1(C1)-Si-O3(C2)	108.8(2)	108.9(3)	109.1(4)	108.4(4)	113.5(5)	111.3(3)	109.2(3)	114.5(4)	115.5(3)	109.7(4)
O2(C1)-Si-O3(C1)	110.2(2)	110.2(3)	109.9(3)	110.6(4)	110.8(5)	110.3(3)	106.9(3)	109.7(4)	110.1(3)	108.1(5)
O2(C1)-Si-O3(C2)	105.4(2)	105.7(3)	106.2(4)	106.7(4)	111.0(4)	107.9(3)	110.3(3)	107.5(40	107.8(4)	108.7(4)
O3(C1)-Si-O3(C2)	107.2(1)	106.6(2)	105.7(3)	105.0(3)	105.2(3)	104.9(2)	104.2(2)	103.0(3)	102.9(2)	102.9(5)
Volume	2.2129	2.2028	2.1882	2.1557	2.1488	2.1104	2.0855	2.057	2.0596	2.0081
Distortion index	0.01046	0.01149	0.01232	0.01096	0.00684	0.01069	0.01194	0.01683	0.00914	0.00772
Quadratic elongation, λ	1.0035	1.0035	1.0029	1.0031	1.0022	1.0022	1.0033	1.0041	1.0043	1.0073
Bond angle variance, σ^2	14.3562	14.5229	11.8588	13.3703	8.6476	8.8378	12.5543	15.2229	16.6721	29.2702
O3-O3-O3	173.5(2)	171.6(3)	168.3(3)	163.9(3)	162.2(4)	158.7(3)	157.9(3)	154.7(3)	155.8(3)	152.7(3)

quadratic elongation are defined as $\sigma^2 = \sum_{i=1}^{n}\left[(\theta_i - \theta_0)^2/(n-1)\right]$ and $\lambda = \sum_{i=1}^{n}\left[(l_i - l_0)^2/n\right]$, where θ_i is the ith angle, θ_0 is the ideal bond angle for a perfect regular polyhedron, l_i is the ith center-to-vertex distance, and l_0 is the center-to-vertex distance of a regular polyhedron. In this study we calculated the values of σ^2 and λ for SiO_4 tetrahedra and FeO_6 octahedra. The evolutions of the values of σ^2 and λ for each coordination polyhedron show similar trends as pressure changes. The σ^2 value of SiO_4 tetrahedra is slowly reduced from the ambient value of 14.36 to 8.84 (for λ value, from 1.0035 to 1.0022) at 24.0(1) GPa, then increased to 29.27 (1.0073 for λ value) at 60.4(1) GPa (Figures 10 and 11). The values of σ^2 and λ for FeO_6 octahedra are more responsive to pressure change than SiO_4 tetrahedra. The λ value reduces from 1.0126 to 1.0114 (for σ^2, from 39.08 to 36.96) at 12.7(1) GPa and rapidly increases to 1.0344 (121.35 for σ^2 value) at 60.4(1) GPa (Figures 10 and 11).

3.3. Compression Mechanism and *C2/c* → *C2/c* Bonding Transition

It is clear that the unit cell compression of aegirine is mainly controlled by reducing volumes of NaO_8 and $Fe^{3+}O_6$ polyhedra (Figure 12). NaO_8 is the most compressible and the most distorted polyhedron at ambient conditions. At ambient conditions, the longest Na-O bond of aegirine is Na-O3(C1, D1), with 2.439(4) Å. The initially unbounded Na-O3(C2, D2) distance is shortened to a comparable length of 2.433(6) Å at 24.0(1) GPa (Table 4). Therefore, aegirine undergoes an *C2/c* → *C2/c* bonding transition as a result of the Na-O3(C2, D2) bond formation which occurs near this pressure, as predicted by *McCarthy et al.* [2008a] and *McCarthy et al.* [2008b]. This bonding transition has several discontinuous consequences: (i) pressure dependence of the β angle (Figure 5) decreases and shows an increase in scatter, (ii) pressure dependence of the tetrahedral chain kinking angle (Figure 13) decreases, (iii) pressure dependence of polyhedral distortion of M2 decreases (Figure 9),

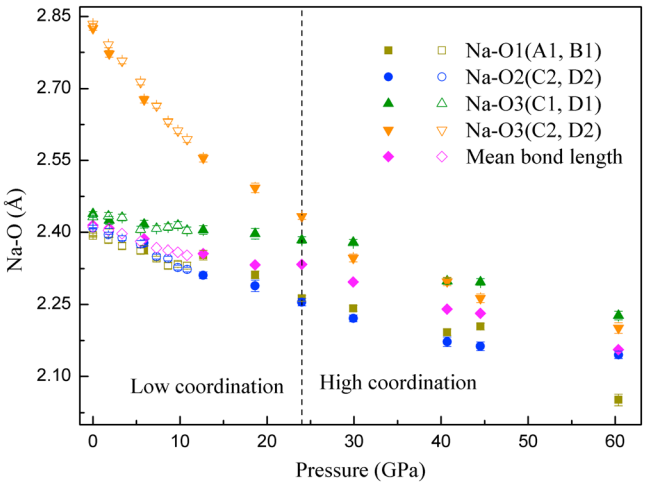

Figure 6. Pressure dependence of Na-O interatomic distances in NaO_8 polyhedron. The solid markers are from this study, and the open markers are from *McCarthy et al.* [2008a]. (*Color online*).

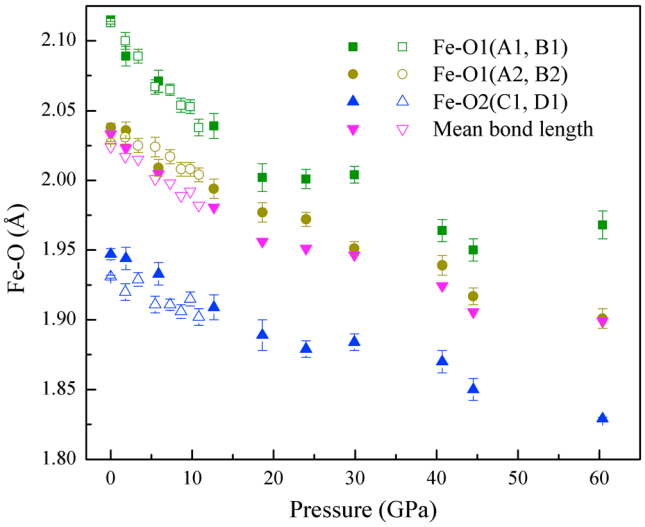

Figure 7. Pressure dependence of Fe-O bond lengths in FeO_8 octahedron. The solid markers are from this study, and the open markers are from *McCarthy et al.* [2008a]. (*Color online*).

and (iv) pressure dependences of bond angle variance (σ^2) and quadratic elongation (λ) of SiO_4 tetrahedra and $Fe^{3+}O_6$ octahedra change (Figures 10 and 11). The two dimensional sheets in (100) plane, built by NaO_8 and $Fe^{3+}O_6$ polyhedra, are sandwiched by SiO_4 tetrahedral chains and run perpendicular to the [100] direction, which is the most incompressible axis. SiO_4 tetrahedral chains have large rotation freedom, which can be expressed by reduction of O3-O3-O3 angle. Tetrahedral chain rotation makes the *c* direction more compressible but requires high deformability of the M2 site. Figures 12 and 13 show that the O3-O3-O3 angle has a discontinuity at 24.0(1) GPa, but the SiO_4-tetrahedral compression does not exhibit discontinuity like in kosmochlor [*Posner et al.*, 2014]. The high compressibility of the *b* direction can be attributed to the projection of long and soft Na-O bonds along this direction.

Isosymmetric, "type 0" phase transitions are not uncommon in mineral physics, and as pointed out by *Christy* [1995], are necessarily first order only when there are no intermediate lower symmetry states, which might not be observed in experiments. Well-known examples of type 0 transitions include pressure-induced layer shift in kaolin-group phyllosilicates [*Dera et al.*, 2003], pressure-induced coordination changes of anorthoclase [*Nestola et al.*, 2008] and kalsilite [$KAlSiO_4$] [*Gatta et al.*, 2011], and spin crossover transitions occurring at high pressure in most of iron-bearing minerals [e.g., *Lin and Tsuchiya*, 2008; *Lin et al.*, 2005; *Speziale et al.*, 2007; *Chen et al.*, 2012]. An isosymmetric high-temperature phase transition was also recently described in orthopyroxene solid solution system [*Ohi and Miyake*, 2016]. In this study the phase transition of aegirine is also isosymmetric, however does not show a discontinuity in the *P-V* curve (Figures 2 and 14) but an obvious change in bulk modulus (Figures 3 and 15), and hence, it has the characteristics of second-order phase transitions. This isosymmetric phase transition of aegirine could be triggered by the coordination change of Na^+ based on above discussions. Moreover, aegirine is also an iron-bearing mineral; therefore, other relevant reasons should be considered. First, these include possibility of magnetic transition. A temperature-induced magnetic transition of aegirine has been described by *Baum et al.* [1997]; in this study the high-pressure conditions could trigger such magnetic change. Pressure-induced magnetic transition of other Fe-bearing minerals like magnetite [Fe_3O_4] has also been reported [*Ding et al.*, 2008]. Second, this second-order phase transition could be due to spin transition of Fe^{3+} in aegirine. Although our data do not fully suggest a complete high-to-low spin transition, aegirine

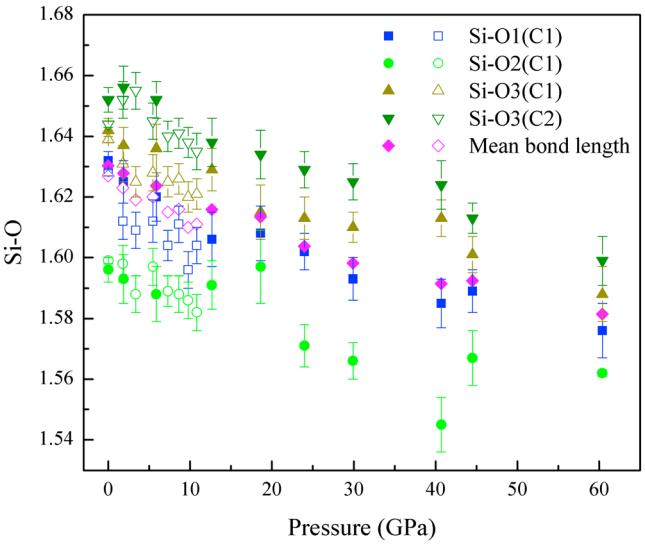

Figure 8. Pressure dependence of Si-O bond lengths in SiO_4 tetrahedron. The solid markers are from this study, and the open markers are from *McCarthy et al.* [2008a]. (*Color online*).

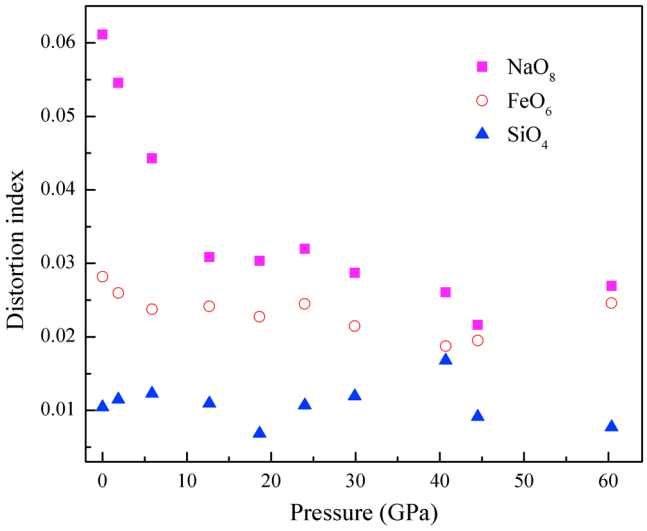

Figure 9. Pressure dependences of distortion indices of different polyhedra (*Color online*).

after ~24 GPa, it is possible to have Fe^{3+} in intermediate spin state, which is similar to the spin transition behavior of Fe^{2+} in magnetite [Fe_3O_4] [*Ding et al.*, 2008]. We also calculated the actual atomic displacements upon this phase transition by mapping the high-pressure *C*2/*c* structure (29.9 GPa) onto the low-pressure *C*2/*c* structure (18.6 GPa) in a normalized cell shape (20.0 GPa). Table 7 shows the computed results. The anions have larger displacements than the cations; Na is larger than other cations, and O1 is smaller than O2 and O3.

Subtle discontinuities of this type of phase transition are easy to overlook experimentally, because they do not cause noticeable changes in the diffraction pattern; however, they often have significant consequences for compression behavior. As can be seen in Figure 2, the bonding transition in aegirine changes the ambient temperature equation of state to the extent that the extrapolation of the low-pressure trend to 60 GPa gives a density difference of about 3%. While most subduction zones do not extend beyond 1000 km depth (corresponding to pressure of about 40 GPa), buoyancy relations within old and cold subduction zones are quite subtle [*Niu et al.*, 2003; *Romanyuk et al.*, 1999; *Ganguly et al.*, 2009; *Tassara and Echaurren*, 2012; *Tassara et al.*, 2006], and density differences of the order of few % may affect whether the subducted slab will be able to penetrate the transition zone or deflect horizontally and stagnate [*Agrusta et al.*, 2014; *King et al.*, 2015]. On the other hand, the 660 km discontinuity is one of the most important boundaries on Earth's interior and has been widely accepted to be controlled by ringwoodite → Mg-perovskite + ferropericlase transformation [*Green and Ringwood*, 1967; *Ito and Takahashi*, 1989; *Liu*, 1976b]. However, different phase transformation model for the explanation and regional anomalies of this discontinuity suggest a more complex model [*Cornwell et al.*, 2011; *Ghosh et al.*, 2013; *Houser and Williams*, 2010; *Jenkins et al.*, 2016; *Wang and Niu*, 2010]. The 24 GPa in this study corresponds almost exactly to the 660 km seismic discontinuity (Figures 14 and 15), and while the bonding transition in aegirine certainly cannot alone explain all of the seismic changes associated with this discontinuity, and the temperature effects still need to be carefully evaluated, based on our findings, Na-bearing clinopyroxene is likely to add its own discontinuous contributions at depths greater than 660 km, if it is present metastably preserved in significant enough quantities.

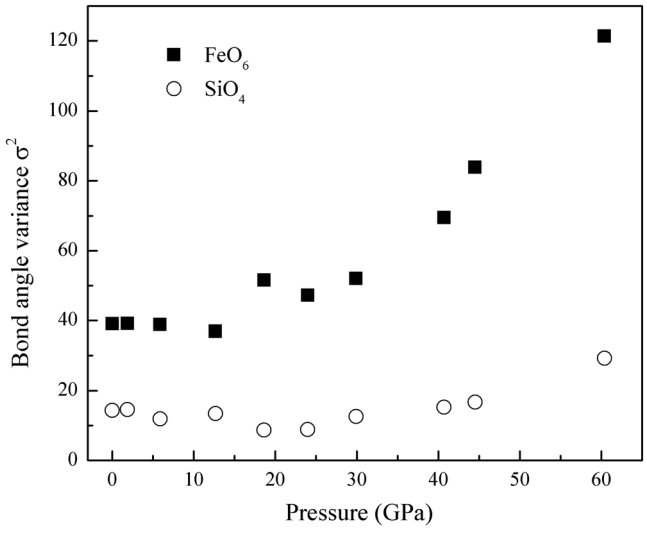

Figure 10. Pressure dependences of bond angle variance (σ^2) value of different polyhedra.

To better assess the contributions of Na-coordination change on discontinuities of deep Earth's interior we calculated the density and bulk modulus profiles of aegirine and jadeite along a geotherm which is typical for cold subduction [*Ganguly et al.*, 2009] (Figures 14 and 15) and compared it with the average mantle preliminary

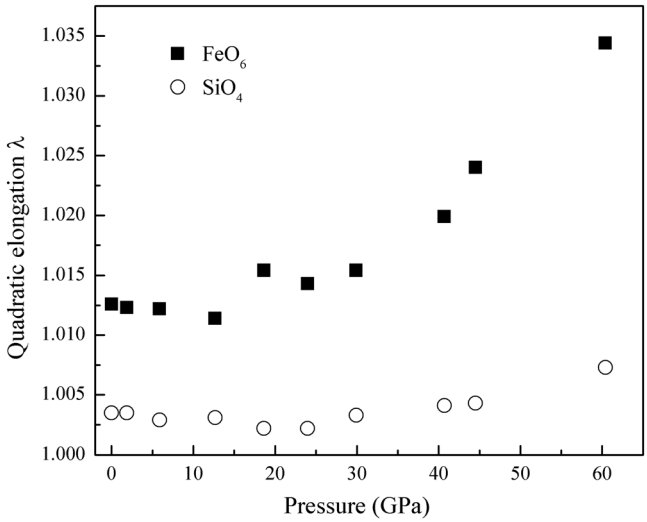

Figure 11. Pressure dependences of quadratic elongation (λ) value of different polyhedra.

reference Earth model (PREM) model [*Dziewonski and Anderson*, 1981]. The third-order high-temperature BM3 equation of state was used for these calculations.

$$P = (3/2)K_{(T,\ 0)}\left[\left(\rho_{(T,\ P)}/\rho_{(T,\ 0)}\right)^{7/3} - \left(\rho_{(T,\ P)}/\rho_{(T,\ 0)}\right)^{5/3}\right] \times \left[1 + (3/4)\left(K'_{(T,\ 0)} - 4\right)\left[\left(\rho_{(T,P)}/\rho_{(T,\ 0)}\right)^{2/3} - 1\right]\right] \quad (2)$$

$$\rho_{(T,\ 0)} = \rho_0 \exp\int_{300}^{T} \alpha_T dT \quad (3)$$

$$K_{(T,\ 0)} = K_0 + \left(\partial K_{(T,\ 0)}/\partial T\right)_P \times (T - 300) \quad (4)$$

$$K'_{(T,0)} = K'_{(300,\ 0)} \quad (5)$$

$$\alpha_T = \alpha_0 \quad (6)$$

where $K_{(T,\ 0)}$, $K'_{(T,\ 0)}$, $\rho_{(T,\ 0)}$, and α_T are bulk modulus, its pressure derivative, density and thermal expansivity at temperature T, and ambient pressure, respectively. Because we did not measure the high-temperature data of aegirine, the value of α_T of aegirine determined by *Tribaudino et al.* [2008] was adopted in our calculations, while $\partial K_{(T,\ 0)}/\partial T$ was assumed to be the same as in jadeite [$NaAlSi_2O_6$] (no data of $\partial K_{(T,\ 0)}/\partial T$ for aegirine is currently available). All values of thermoelastic parameters of jadeite were taken from *Zhao et al.* [1997]. Due to the necessity to use the value of $\partial K_{(T,\ 0)}/\partial T$ of jadeite for aegirine, we evaluated the possible influences of this assumption. The difference of $\partial K_{(T,\ 0)}/\partial T$ between aegirine and jadeite is caused by the substitution between Fe^{3+} and Al^{3+}. As no such thermodynamic data for pyroxene minerals are available, we reduced this issue to the influence of the substitution of Al^{3+}/Fe^{3+} on the value of $\partial K_{(T,\ 0)}/\partial T$ in silicates, and we referenced garnet data to assess the extent of the effect. *Pavese et al.* [2001] investigated thermal equations of state on approximately end-member andradite [$Ca_{3.00}(Al_{0.03}Fe^{3+}_{1.97})$

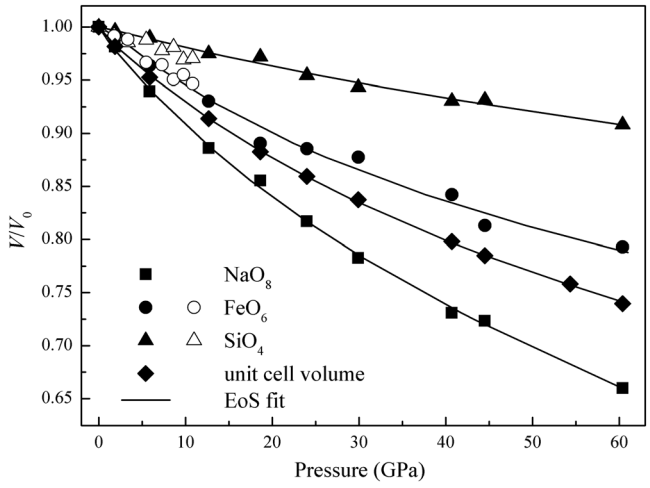

Figure 12. Pressure dependences of polyhedra and unit cell volume. The solid markers are from this study, and the open markers are from *McCarthy et al.* [2008a]. The error bars of the data points are smaller than the symbols.

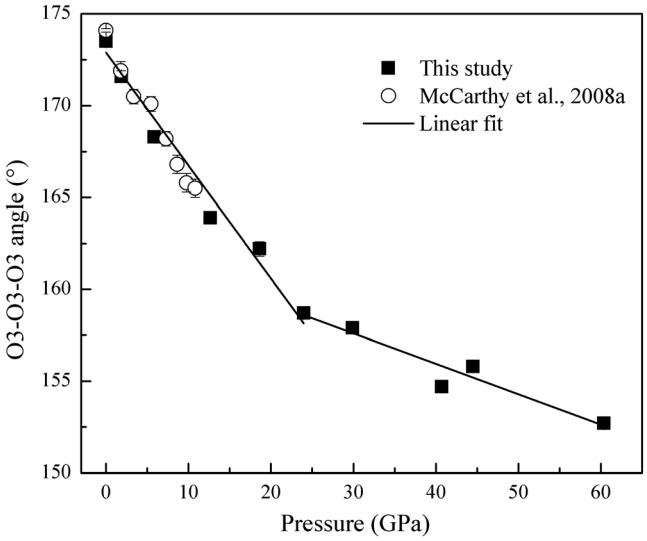

Figure 13. Tetrahedral chain kinking as described byO3-O3-O3 angle in aegirine as a function of pressure.

$Si_{3.00}O_{12}$] and grossular [$(Ca_{2.90}Fe^{2+}_{0.10})(Mn_{0.01}Al_{1.95}Ti_{0.04})Si_{2.99}O_{12}$], and obtained values of $\partial K_{(T,\ 0)}/\partial T$ are −0.020(3) and −0.016(3), respectively. We used the difference between andradite and grossular to evaluate similar effect in clinopyroxenes. We concluded that calculations based on this assumption would give smaller values of density but larger bulk moduli. At a depth of 900 km it will produce differences of 0.5% and 2% for density and bulk modulus, respectively. Furthermore, it should be noted that other errors would also be introduced because these two garnets are not pure end-members and structures of garnet and pyroxene are different.

Aegirine and jadeite represent the most Na-rich compositions of pyroxene family, which are not expected to be present in large quantities in the average pyrolytic mantle. The subducted slab, on the other hand, with its layered structure consisting of basalt on the top, harzburgite in the middle, and lherzolite at the bottom [*Ganguly et al*., 2009], contains appreciable amount of Na-rich minerals, including clinopyroxenes in the basaltic region. For example, eclogite, to which basalt metamorphises below 100 km, has a high content of Na-rich omphacite clinopyroxene. According to phase equilibria modeling [*Ganguly et al*., 2009] subducted basalt will preserve approximately 10 wt % of clinopyroxene to 800 km depth.

As can be seen in Figure 14, at 660 km there is a dramatic increase in the density of pyrolytic PREM mantle due to the formation of bridgmanite. Below this depth, the slab is denser than the mantle, which results in negative buoyancy and sinking. At the 660 km boundary, the slab and surrounding mantle densities become comparable, and the buoyancy relation becomes very sensitive to factors such as chemical changes and metastable phase transitions. Aegirine is noticeably denser than jadeite because of replacement of Al^{3+} with Fe^{3+} which is twice as heavy. Density of jadeite is very close to the density of PREM pyrolite in the olivine-rich region, between 200 and 400 km. In the same region aegirine is approximately 7% denser. When olivine transforms to higher-pressure β and γ polymorphs, the PREM density becomes comparable to that of aegirine, and much denser than jadeite. The coordination change in aegirine has only a minor effect on density, but the effect would cause a slight increase in buoyancy, thus weakly promoting slab stagnation.

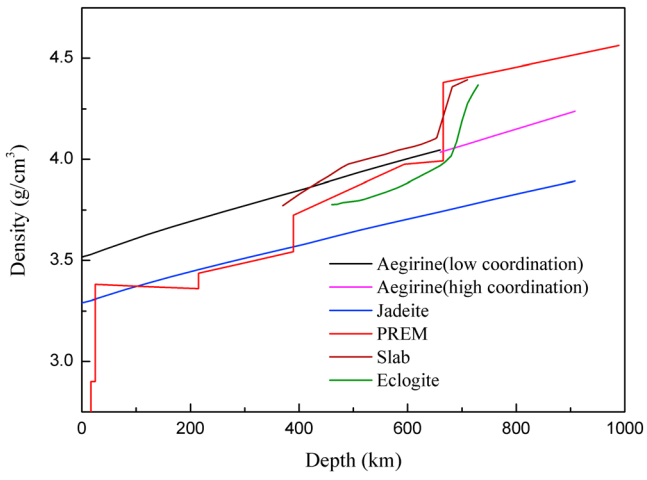

Figure 14. Calculated density profiles of aegirine and jadeite to ~1000 km, and the PREM [*Dziewonski and Anderson*, 1981] and the density profile of a Tonga-type slab [*Ganguly et al*., 2009] are also showed. The eclogite profile is calculated along the 1400°C adiabat [*Anderson and Bass*, 1986] (*Color online*).

The changes in bulk modulus as a function depth, shown in Figure 15, can be interpreted in terms of the effect on seismic compressional wave velocity contrast between the slab and the surrounding mantle, according to the

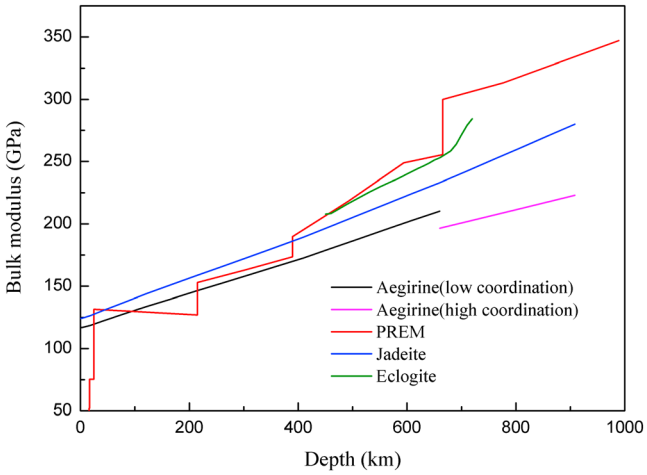

Figure 15. Calculated bulk modulus profiles of aegirine and jadeite along with PREM [*Dziewonski and Anderson*, 1981] to ~1000 km, and the eclogite profile is calculated along the 1400°C adiabat [*Anderson and Bass*, 1986] (*Color online*).

Newton-Laplace equation approximation. The 660 km discontinuity coincides almost exactly with the Na coordination change in aegirine, but this transformation has an opposite effect on the bulk modulus, lowering it discontinuously, as compared to the perovskite formation in mantle pyrolite, which causes a significant increase of the bulk modulus. As a result, the presence of metastable Na-clinopyroxene at 660 km would increase the seismic contrast between the slab and the surrounding mantle.

4. Conclusions

We carried out high-pressure single-crystal X-ray diffraction experiments on a natural Na, Fe *C*2/*c* clinopyroxene [$NaFe^{3+}Si_2O_6$] to ~60 GPa. Bulk modulus and its pressure derivative were determined to be 126(2) GPa and 3.3(1) by fitting third-order Birch-Murnaghan equation of state to all experimental data. Unit strain ellipsoid analysis indicates that ε_1:ε_2:ε_3 is 1.00:2.44:1.64. Careful analysis of structural data and f_E-F_E plot clearly indicates a change in the compression mechanism, related to new bond formation at the M2 site.

Unlike orthopyroxenes, which have been shown to undergo a series of subtle displacive, symmetry-changing phase transitions at ambient temperature and pressure above 10 GPa [e.g., *Dera et al*., 2013a; *Finkelstein et al*., 2015; *Zhang et al*., 2013; *Zhang et al*., 2012], clinopyroxenes, once locked in the *C*2/*c* structure, seem to prefer retaining this structural arrangement at ambient temperature to much higher pressures. In this respect aegirine behaves just like diopside and hedenbergite. However, unlike diopside and hedenbergite, where higher-pressure phases have been reported above 50 GPa [*Plonka et al*., 2012; *Zhang et al*., 1999], aegirine remains in the *C*2/*c* structure up to at least 60 GPa, which can be attributed to the behavior of the Na^+ cation with ionic radius larger than Mg^{2+}, Fe^{2+}, or Ca^{2+}. Aegirine undergoes the isosymmetric *C*2/*c* → *C*2/*c* bonding transition deriving from the Na-O3(C2, D2) bond formation at pressure of about 24 GPa. The NaO_8 polyhedron has the highest volume and compressibility, and controls the compression mechanism. The distortion index of NaO_8 polyhedron initially decreases rapidly as pressure increases, and then at around 24 GPa becomes less responsive to pressure changes, as the longest, most compressible Na-O3(C2, D2) contacts are bonded and become comparable in length to the remaining bonds in the M2 polyhedron. This inflection point causes significant changes in the pressure slope of distortion index for M2, tetrahedral kinking angle, monoclinic βangle, and volume compressibility. While there is no change in symmetry, the compressional behavior of aegirine below 20 GPa and above that pressure is quite different because of the bonding transition, making extrapolations based exclusively on low-pressure experiments quite inaccurate.

Such subtle changes in the details of the crystal structure of major mantle minerals at depth may not seem to be particularly impactful at first sight; however, a number of earlier studies demonstrated clear links and appreciable predictive power of coordination-polyhedron geometry and compressibility-based methods to explain trends in the most important thermodynamic parameters including entropy, enthalpy, [*Van Hinsberg et al*., 2005a; *Chermak and Rimstidt*, 1989], elastic moduli [*Webb and Jackson*, 1990], heat capacity, thermal expansion [*Van Hinsberg et al*., 2005b], and partitioning coefficients [*Wood and Blundy*, 1997] across

Table 7. Atomic Displacements Occurred Upon Phase Transition in Aegirine Crystal Structure

Atoms	Na	Fe	Si	O1	O2	O3
Atomic displacements (Å)	0.03	0.01	0.02	0.06	0.07	0.07

solid solution series. By the same token, we expect that all of these parameters will be affected by the bonding transition in jadeite-aegirine series at about 24 GPa.

Aegirine may not be the most common of clinopyroxenes in subduction zones, but it is relevant as the end-member of the jadeite-aegirine solid solution, which plays relevant role in the blueschist-eclogite transformation, prominent in subduction zone environments. McCarthy et al. classified both aegirine and jadeite in the same category of pyroxenes with antipathetic bonds [*McCarthy et al*., 2008a] and predict both end-members to display the same Na M2 site coordination number increase at about 20 GPa. The highest-pressure jadeite study [*Posner et al*., 2014] did not quite reach high-enough pressure to assess the discontinuous effects of the bonding change; thus, the current aegirine results provide the most accurate to-date assessment of what to expect across the solid solution. Because of this compressional behavior duality, in order to better understand the properties of metastable pyroxene-containing rocks in the deeper parts of the cold subduction zones we need more systematic studies of clinopyroxene minerals at pressures well exceeding 20 GPa.

Acknowledgments

This experimental work was performed at GeosoliEnviroCARS (Sector 13), Advanced Photon Source, and Argonne National Laboratory. GeosoliEnviroCARS is supported by the National Science Foundation–Geosciences (EAR-1128799) and the Department of Energy–Geosciences (DE-FG02-94ER14466). PX^2 program is supported by COMPRES under NSF Cooperative Agreement EAR 11-57758. The use of the COMPRES-GSECARS gas loading system was supported by COMPRES under NSF Cooperative Agreement EAR-1157758 and by GSECARS. The project was supported by the National Science Foundation under grant EAR-1344942 and National Natural Science Foundation of China (grant 41374107). The development of the ATREX software used for data analysis is supported by NSF grant EAR-1440005.The use of the Advanced Photon Source was supported by the US Department of Energy, Office of Science, Office of Basic Energy Sciences, under contract DE-AC02-06CH11357. J. Xu acknowledges supports from the Strategic Priority Research Program (B) of the Chinese Academy of Sciences (XDB 18010401) and Graduate Student Joint Training Program of the Institute of Geochemistry, Chinese Academy of Sciences. We would like to thank Oliver Tschauner and the other anonymous reviewer for their thorough and helpful comments, which help to improve the quality of this manuscript. We would like to thank Michael Walter for handling this manuscript. The data for this paper are available by contacting the corresponding author at the University of Hawai'i at Mānoa, USA (pdera@hawaii.edu).

References

Agrusta, R., J. Hunen, and S. Goes (2014), The effect of metastable pyroxene on the slab dynamics, *Geophys. Res. Lett.*, *41*, 8800–8808, doi:10.1002/2014GL062159.

Akashi, A., Y. Nishihara, E. Takahashi, Y. Nakajima, Y. Tange, and K. I. Funakoshi (2009), Orthoenstatite/clinoenstatite phase transformation in $MgSiO_3$ at high-pressure and high-temperature determined by in situ X-ray diffraction: Implications for nature of the X discontinuity, *J. Geophys. Res.*, *114*, B04206, doi:10.1029/2008JB005894.

Akimoto, S.-I., and Y. Syono (1970), High-pressure decomposition of the system $FeSiO_3$-$MgSiO_3$, *Phys. Earth Planet. Inter.*, *3*, 186–188.

Anderson, D. L., and J. D. Bass (1986), Transition region of the Earth's upper mantle, *Nature*, *320*(6060), 321–328.

Angel, R. J. (2000), Equations of state, *Rev. Miner. Geochem.*, *41*(1), 35–59.

Angel, R. J., J. Gonzalez-Platas, and M. Alvaro (2014), EosFit7c and a Fortran module (library) for equation of state calculations, *Z. Kristallogr.*, *229*(5), 405–419, doi:10.1515/zkri-2013-1711.

Angiboust, S., P. Agard, J. Glodny, J. Omrani, and O. Oncken (2016), Zagros blueschists: Episodic underplating and long-lived cooling of a subduction zone, *Earth Planet. Sci. Lett.*, *443*, 48–58, doi:10.1016/j.epsl.2016.03.017.

Baum, E., W. Treutmann, W. Lottermoser, and G. Amthauer (1997), Magnetic properties of the clinopyroxenes aegirine and hedenbergite: A magnetic susceptibility study on single crystals, *Phys. Chem. Miner.*, *24*(4), 294–300, doi:10.1007/s002690050041.

Baur, W. (1974), The geometry of polyhedral distortions. Predictive relationships for the phosphate group, *Acta Crystallogr.*, *B30*, 1195–1215.

Bina, C. R., and A. Navrotsky (2000), Possible presence of high-pressure ice in cold subducting slabs, *Nature*, *408*(6814), 844–847, doi:10.1038/35048555.

Bina, C. R., S. Stein, F. C. Marton, and E. M. Van Ark (2001), Implications of slab mineralogy for subduction dynamics, *Phys. Earth Planet. Inter.*, *127*(1), 51–66.

Cameron, M., S. Sueno, C. T. Prewitt, and J. J. Papike (1973), High-temperature crystal chemistry of acmite, diopside, hedenbergite, jadeite, spodumene, and ureyite, *Am. Miner.*, *58*, 594–618.

Chen, B., J. M. Jackson, W. Sturhahn, D. Zhang, J. Zhao, J. K. Wicks, and C. A. Murphy (2012), Spincrossover equation of state and sound velocities of $(Mg_{0.65}Fe_{0.35})O$ ferropericlase to 140 GPa, *J. Geophys. Res.*, *117*, B08208, doi:10.1029/2012JB009162.

Chermak, J. A., and J. D. Rimstidt (1989), Estimating the thermodynamic properties (ΔG_f^0 and ΔH_f^0) of silicate minerals at 298 K from the sum of polyhedral contributions, *Am. Miner.*, *74*, 1023–1031.

Christy, A. G. (1995), Isosymmetric structural phase transitions: Phenomenology and examples, *Acta Crystallogr.*, *51*(5), 753–757.

Clark, J. R., D. E. Appleman, and J. Papike (1969), Crystal-chemical characterization of clinopyroxenes based on eight new structure refinements, *Mineral. Soc. Am.*, *2*, 31–50.

Cornwell, D., G. Hetényi, and T. Blanchard (2011), Mantle transition zone variations beneath the Ethiopian Rift and Afar: Chemical heterogeneity within a hot mantle?, *Geophys. Res. Lett.*, *38*, L16308, doi:10.1029/2011GL047575.

Cortesogno, L., L. Gaggero, G. Lucchetti, and R. Cabella (2002), Compositions and miscibility gap in Na-Ca clinopyroxenes through highpressure metamorphism, *Period. Mineral.*, *71*, 1–25.

Dera, P., C. T. Prewitt, S. Japel, D. L. Bish, and C. T. Johnston (2003), Pressure-controlled polytypism in hydrous layered materials, *Am. Miner.*, *88*(10), 1428–1435.

Dera, P., G. J. Finkelstein, T. S. Duffy, R. T. Downs, Y. Meng, V. Prakapenka, and S. Tkachev (2013a), Metastable high-pressure transformations of orthoferrosilite Fs 82, *Phys. Earth Planet. Inter.*, *221*, 15–21.

Dera, P., K. Zhuravlev, V. Prakapenka, M. L. Rivers, G. J. Finkelstein, O. Grubor-Urosevic, O. Tschauner, S. M. Clark, and R. T. Downs (2013b), High pressure single-crystal micro X-ray diffraction analysis with GSE_ADA/RSV software, *High Pressure Res.*, *33*(3), 466–484.

Ding, Y., D. Haskel, S. G. Ovchinnikov, Y.-C. Tseng, Y. S. Orlov, J. C. Lang, and H.-k. Mao (2008), Novel pressure-induced magnetic transition in magnetite (Fe_3O_4), *Phys. Rev. Lett.*, *100*(4), 045508, doi:10.1103/PhysRevLett.100.045508.

Dolomanov, O. V., L. J. Bourhis, R. J. Gildea, J. A. Howard, and H. Puschmann (2009), OLEX2: A complete structure solution, refinement and analysis program, *J. Appl. Crystallogr.*, *42*(2), 339–341.

Downs, R. T. (2003), Topology of the pyroxenes as a function of temperature, pressure, and composition as determined from the procrystal electron density, *Am. Miner.*, *88*(4), 556–566.

Downs, R. T., and A. K. Singh (2006), Analysis of deviatoric stress from nonhydrostatic pressure on a single crystal in a diamond anvil cell: The case of monoclinic aegirine, $NaFeSi_2O6$, *J. Phys. Chem. Solids*, *67*(9–10), 1995–2000, doi:10.1016/j.jpcs.2006.05.035.

Dziewonski, A. M., and D. L. Anderson (1981), Preliminary reference Earth model, *Phys. Earth Planet. Inter.*, *25*(4), 297–356.

Farrugia, L. J. (2012), WinGX and ORTEP for Windows: An update, *Appl. Crystallogr.*, *45*(4), 849–854.

Finkelstein, G. J., P. K. Dera, and T. S. Duffy (2015), Phase transitions in orthopyroxene (En(90)) to 49 GPa from single-crystal X-ray diffraction, *Phys. Earth Planet. Inter.*, *244*, 78–86.

Frost, D. J. (2008), The upper mantle and transition zone, *Elements*, *4*(3), 171–176, doi:10.2113/gselements.4.3.171.

Ganguly, J., A. M. Freed, and S. K. Saxena (2009), Density profiles of oceanic slabs and surrounding mantle: Integrated thermodynamic and thermal modeling, and implications for the fate of slabs at the 660 km discontinuity, *Phys. Earth. Planet. Inter.*, *172*(3), 257–267.
Gatta, G., R. J. Angel, J. Zhao, M. Alvaro, N. Rotiroti, and M. A. Carpenter (2011), Phase stability, elastic behavior, and pressure-induced structural evolution of kalsilite: A ceramic material and high-T/high-P mineral, *Am. Miner.*, *96*(8–9), 1363–1372.
Ghosh, S., E. Ohtani, K. D. Litasov, A. Suzuki, D. Dobson, and K. Funakoshi (2013), Effect of water in depleted mantle on post-spinel transition and implication for 660 km seismic discontinuity, *Earth Planet. Sci. Lett.*, *371*, 103–111.
Green, D., and A. Ringwood (1967), The stability fields of aluminous pyroxene peridotite and garnet peridotite and their relevance in upper mantle structure, *Earth Planet. Sci. Lett.*, *3*, 151–160.
Houser, C., and Q. Williams (2010), Reconciling Pacific 410 and 660 km discontinuity topography, transition zone shear velocity patterns, and mantle phase transitions, *Earth Planet. Sci. Lett.*, *296*(3), 255–266.
Ito, E., and E. Takahashi (1989), Postspinel transformations in the system Mg_2SiO_4-Fe_2SiO_4 and some geophysical implications, *J. Geophys. Res.*, *94*(B8), 10,637–10,646, doi:10.1029/JB094iB08p10637.
Jahn, S. (2008), High-pressure phase transitions in $MgSiO_3$ orthoenstatite studied by atomistic computer simulation, *Am. Miner.*, *93*(4), 528–532, doi:10.2138/am.2008.2710.
Jenkins, J., S. Cottaar, R. White, and A. Deuss (2016), Depressed mantle discontinuities beneath Iceland: Evidence of a garnet controlled 660 km discontinuity?, *Earth Planet. Sci. Lett.*, *433*, 159–168.
Kantor, I., V. Prakapenka, A. Kantor, P. Dera, A. Kurnosov, S. Sinogeikin, N. Dubrovinskaia, and L. Dubrovinsky (2012), BX90: A new diamond anvil cell design for X-ray diffraction and optical measurements, *Rev. Sci. Instrum.*, *83*(12), 125102, doi:10.1063/1.4768541.
King, S. D., D. J. Frost, and D. C. Rubie (2015), Why cold slabs stagnate in the transition zone, *Geology*, *43*(3), 231–234.
Kung, J., B. S. Li, T. Uchida, Y. B. Wang, D. Neuville, and R. C. Liebermann (2004), In situ measurements of sound velocities and densities across the orthopyroxene-high-pressure clinopyroxene transition in MgSiO3 at high pressure, *Phys. Earth Planet. Inter.*, *147*(1), 27–44, doi:10.1016/j.pepi.2004.05.008.
Lin, J.-F., and T. Tsuchiya (2008), Spin transition of iron in the Earth's lower mantle, *Phys. Earth Planet. Inter.*, *170*(3), 248–259.
Lin, J.-F., V. V. Struzhkin, S. D. Jacobsen, M. Y. Hu, P. Chow, J. Kung, H. Liu, H.-k. Mao, and R. J. Hemley (2005), Spin transition of iron in magnesiowüstite in the Earth's lower mantle, *Nature*, *436*(7049), 377–380.
Liu, L.-G. (1976a), The high-pressure phases of $FeSiO_3$ with implications for Fe_2 SiO_4 and FeO, *Earth Planet. Sci. Lett.*, *33*(1), 101–106.
Liu, L.-G. (1976b), The post-spinel phase of forsterite, *Nature*, *262*, 770–772.
Mao, H., J.-A. Xu, and P. Bell (1986), Calibration of the ruby pressure gauge to 800 kbar under quasi-hydrostatic conditions, *J. Geophys. Res.*, *91*(B5), 4673–4676, doi:10.1029/JB091iB05p04673.
McCarthy, A. C., R. T. Downs, R. M. Thompson, and G. J. Redhammer (2008a), In situ high-pressure single-crystal X-ray study of aegirine, $NaFe^{3+}Si_2O_6$, and the role of M1 size in clinopyroxene compressibility, *Am. Miner.*, *93*(11-12), 1829–1837, doi:10.2138/am.2008.2725.
McCarthy, A. C., R. T. Downs, and R. M. Thompson (2008b), Compressibility trends of the clinopyroxenes, and in-situ high-pressure single-crystal X-ray diffraction study of jadeite, *Am. Miner.*, *93*(1), 198–209.
Ming, L.-C., and W. A. Bassett (1975), High-pressure phase transformations in the system of $MgSiO_3$-$FeSiO_3$, *Earth Planet. Sci. Lett.*, *27*(1), 85–89.
Nestola, F., T. B. Ballaran, C. Liebske, M. Bruno, and M. Tribaudino (2006), High-pressure behaviour along the jadeite NaAlSi2O6-aegirine NaFeSi2O6 solid solution up to 10 GPa, *Phys. Chem. Miner.*, *33*(6), 417–425, doi:10.1007/s00269-006-0089-7.
Nestola, F., N. Curetti, G. Ivaldi, R. J. Angel, and E. Bruno (2008), Compressibility and high-pressure behavior of $Ab_{63}Or_{27}An_{10}$ anorthoclase, *Can. Miner.*, *46*(6), 1443–1454.
Nestola, F., T. B. Ballaran, R. J. Angel, J. Zhao, and H. Ohashi (2010), High-pressure behavior of Ca/Na clinopyroxenes: The effect of divalent and trivalent 3d-transition elements, *Am. Miner.*, *95*(5–6), 832–838, doi:10.2138/am.2010.3396.
Nishi, M., T. Kato, T. Kubo, and T. Kikegawa (2008), Survival of pyropic garnet in subducting plates, *Phys. Earth Planet. Inter.*, *170*(3), 274–280.
Nishi, M., T. Kubo, H. Ohfuji, T. Kato, Y. Nishihara, and T. Irifune (2013), Slow Si–Al interdiffusion in garnet and stagnation of subducting slabs, *Earth Planet. Sci. Lett.*, *361*, 44–49.
Niu, Y., M. J. O'Hara, and J. A. Pearce (2003), Initiation of subduction zones as a consequence of lateral compositional buoyancy contrast within the lithosphere: A petrological perspective, *J. Petrol.*, *44*(5), 851–866.
Ohashi, Y. (1982), STRAIN, a program to calculate the strain tensor from two sets of unit-cell parameters, in *Comparative Crystal Chemistry*, edited by R. M. Hazen and L. W. Finger, pp. 92–102, Wiley, New York.
Ohi, S., and A. Miyake (2016), Phase transitions between high-and low-temperature orthopyroxene in the $Mg_2Si_2O_6$-$Fe_2Si_2O_6$ system, *Am. Miner.*, *101*(6), 1414–1422.
Pavese, A., V. Diella, V. Pischedda, M. Merli, R. Bocchio, and M. Mezouar (2001), Pressure–volume–temperature equation of state of andradite and grossular, by high-pressure and -temperature powder diffraction, *Phys. Chem. Miner.*, *28*(4), 242–248, doi:10.1007/s002690000144.
Plonka, A. M., P. Dera, P. Irmen, M. L. Rivers, L. Ehm, and J. B. Parise (2012), β-diopside, a new ultrahigh-pressure polymorph of $CaMgSi_2O_6$with six-coordinated silicon, *Geophys. Res. Lett.*, *39*, L24307, doi:10.1029/2012GL054023.
Posner, E. S., P. Dera, R. T. Downs, J. D. Lazarz, and P. Irmen (2014), High-pressure single-crystal X-ray diffraction study of jadeite and kosmochlor, *Phys. Chem. Miner.*, *41*(9), 695–707, doi:10.1007/s00269-014-0684-y.
Ringwood, A. (1967), The pyroxene-garnet transformation in the Earth's mantle, *Earth. Planet. Sci. Lett.*, *2*(3), 255–263.
Ringwood, A. E. (1975), *Composition and Petrology of the Earth's Mantle*, McGraw-Hill Inc., New York.
Ringwood, A. E. (1982), Phase transformations and differentiation in subducted lithosphere: Implications for mantle dynamics, basalt petrogenesis, and crustal evolution, *J. Geol.*, *90*, 611–643.
Rivers, M., V. B. Prakapenka, A. Kubo, C. Pullins, C. M. Holl, and S. D. Jacobsen (2008), The COMPRES/GSECARS gas-loading system for diamond anvil cells at the Advanced Photon Source, *High Pressure Res.*, *28*(3), 273–292.
Robinson, K., G. Gibbs, and P. Ribbe (1971), Quadratic elongation: A quantitative measure of distortion in coordination polyhedra, *Science*, *172*(3983), 567–570.
Romanyuk, T., H.-J. Götze, and P. Halvorson (1999), A density model of the Andean subduction zone, *Leading Edge*, *18*(2), 264–268.
Shannon, R. (1976), Revised effective ionic radii and systematic studies of interatomic distances in halides and chalcogenides, *Acta Crystallogr. Sec. A*, *32*, 751–767.
Sheldrick, G. M. (2007), A short history of SHELX, *Acta Crystallogr.*, *64*(1), 112–122.
Speziale, S., V. Lee, S. Clark, J. Lin, M. Pasternak, and R. Jeanloz (2007), Effects of Fe spin transition on the elasticity of (Mg, Fe) O magnesiowüstites and implications for the seismological properties of the Earth's lower mantle, *J. Geophys. Res.*, *112*, B10212, doi:10.1029/2006JB004730.
Stixrude, L., and C. Lithgow-Bertelloni (2007), Influence of phase transformations on lateral heterogeneity and dynamics in Earth's mantle, *Earth Planet. Sci. Lett.*, *263*(1–2), 45–55, doi:10.1016/j.epsl.2007.08.027.

Tassara, A., and A. Echaurren (2012), Anatomy of the Andean subduction zone: Three-dimensional density model upgraded and compared against global-scale models, *Geophys. J. Inter.*, *189*(1), 161–168.

Tassara, A., H. J. Götze, S. Schmidt, and R. Hackney (2006), Three-dimensional density model of the Nazca plate and the Andean continental margin, *J. Geophys. Res.*, *111*, B09404, doi:10.1029/2005JB003976.

Tribaudino, M., F. Nestola, M. Bruno, T. B. Ballaran, and C. Liebske (2008), Thermal expansion along the $NaAlSi_2O_6$–$NaFe^{3+}Si_2O_6$ and $NaAlSi_2O_6$–$CaFe^{2+}Si_2O_6$ solid solutions, *Phys. Chem. Miner.*, *35*(5), 241–248, doi:10.1007/s00269-008-0217-7.

Van Hinsberg, V., S. Vriend, and J. Schumacher (2005a), A new method to calculate end-member thermodynamic properties of minerals from their constituent polyhedra I: Enthalpy, entropy and molar volume, *J. Metamorph. Geol.*, *23*(3), 165–179.

Van Hinsberg, V., S. Vriend, and J. Schumacher (2005b), A new method to calculate end-member thermodynamic properties of minerals from their constituent polyhedra II: Heat capacity, compressibility and thermal expansion, *J. Metamorph. Geol.*, *23*(8), 681–693.

Van Mierlo, W., F. Langenhorst, D. Frost, and D. Rubie (2013), Stagnation of subducting slabs in the transition zone due to slow diffusion in majoritic garnet, *Nat. Geosci.*, *6*(5), 400–403.

Vinet, P., J. Ferrante, J. R. Smith, and J. H. Rose (1986), A universal equation of state for solids, *J. Phys. C: Solid State Phys.*, *19*(20), L467–L473, doi:10.1088/0022-3719/19/20/001.

Vinet, P., J. Ferrante, J. H. Rose, and J. R. Smith (1987), Compressibility of solids, *J. Geophys. Res.*, *92*, 9319–9325, doi:10.1029/JB092iB09p09319.

Wang, B., and F. Niu (2010), A broad 660 km discontinuity beneath northeast China revealed by dense regional seismic networks in China, *J. Geophys. Res.*, *115*, B06308, doi:10.1029/2009JB006608.

Webb, S. L., and I. Jackson (1990), Polyhedral rationalization of variation among the single-crystal elastic moduli for the upper-mantle silicates garnet, olivine, and orthopyroxene, *Am. Miner.*, *75*, 731–738.

Wood, B. J., and J. D. Blundy (1997), A predictive model for rare earth element partitioning between clinopyroxene and anhydrous silicate melt, *Contrib. Mineral. Petrol.*, *129*(2–3), 166–181.

Woodland, A. B. (1998), The orthorhombic to high-P monoclinic phase transition in Mg-Fe pyroxenes: Can it produce a seismic discontinuity?, *Geophys. Res. Lett.*, *25*(8), 1241–1244, doi:10.1029/98GL00857.

Woodland, A. B., and R. J. Angel (1997), Reversal of the orthoferrosilite-high-P clinoferrosilite transition, a phase diagram for FeSiO3 and implications for the mineralogy of the Earth's upper mantle, *Eur. J. Miner.*, *9*, 245–254.

Zhang, D., J. M. Jackson, B. Chen, W. Sturhahn, J. Zhao, J. Yan, and R. Caracas (2013), Elasticity and lattice dynamics of enstatite at high pressure, *J. Geophys. Res. Solid Earth*, *118*, 4071–4082, doi:10.1002/jgrb.50303.

Zhang, D. Z., J. M. Jackson, W. Sturhahn, and Y. M. Xiao (2011), Local structure variations observed in orthoenstatite at high pressures, *Am. Miner.*, *96*(10), 1585–1592, doi:10.2138/am.2011.3721.

Zhang, J. S., P. Dera, and J. D. Bass (2012), A new high-pressure phase transition in natural Fe-bearing orthoenstatite, *Am. Miner.*, *97*(7), 1070–1074.

Zhang, L., H. Ahsbahs, S. S. Hafner, and A. Kutoglu (1997), Single-crystal compression and crystal structure of clinopyroxene up to 10 GPa, *Am. Miner.*, *82*(3), 245–258.

Zhang, L., J. Stanek, S. Hafner, H. Ahsbahs, H. Grünsteudel, and J. Metge (1999), 57Fe nuclear forward scattering of synchrotron radiation in hedenbergite $CaFeSi_2O_6$ at hydrostatic pressures up to 68 GPa, *Am. Miner.*, *84*(3), 447–453.

Zhao, Y., R. B. Von Dreele, T. J. Shankland, D. J. Weidner, J. Zhang, Y. Wang, and T. Gasparik (1997), Thermoelastic equation of state of jadeite $NaAlSi_2O_6$: An energy-dispersive Reitveld Refinement Study of low symmetry and multiple phases diffraction, *Geophys. Res. Lett.*, *24*(1), 5–8, doi:10.1029/96GL03769.